Laser guide star Shack-Hartmann wavefront sensor modeling: matched filtering, wavefront sensor nonlinearity, and impact of sodium layer variability for the Thirty Meter Telescope

Luc Gilles, Brent Ellerbroek

Luc Gilles, Brent Ellerbroek, "Laser guide star Shack-Hartmann wavefront sensor modeling: matched filtering, wavefront sensor nonlinearity, and impact of sodium layer variability for the Thirty Meter Telescope," Proc. SPIE 6272, Advances in Adaptive Optics II, 62721A (28 June 2006); doi: 10.1117/12.671486

SPIE.

Event: SPIE Astronomical Telescopes + Instrumentation, 2006, Orlando, Florida , United States

Laser guide star Shack-Hartmann wavefront sensor modeling: matched filtering, wavefront sensor nonlinearity, and impact of sodium layer variability for the Thirty Meter Telescope

Luc Gilles[a] and Brent Ellerbroek[a]

[a]Thirty Meter Telescope Project Office
1200 E. California Boulevard, Mail Code 102-8
Pasadena, CA 91125

ABSTRACT

This paper describes modeling and simulation results for the Thirty Meter Telescope on the degradation of sodium laser guide star Shack-Hartmann wavefront sensor measurement accuracy that will occur due to the spatial structure and temporal variations of the mesospheric sodium layer. Using a contiguous set of LIDAR measurements of the sodium profile, the performance of a standard centroid and of a more refined noise-optimal matched filter spot position estimation algorithm is analyzed and compared for a nominal mean signal level equal to 1000 photo-detected electrons per subaperture per integration time, as a function of subaperture to laser launch telescope distance and CCD pixel read out noise. Both algorithms are compared in terms of their rms spot position estimation error due to noise, their associated wavefront error when implemented on the Thirty Meter Telescope facility adaptive optics system, their linear dynamic range and their bias when detuned from the current sodium profile.

Keywords: Sodium laser guide star elongation, wavefront sensing, dynamic range, nonlinearity

1. INTRODUCTION

The mesospheric sodium layer is located at a mean altitude of $h_{\rm Na} = 90$ km and has a mean thickness of $\sigma_{\rm Na} = 10$ km. As a result, a sodium laser guide star (LGS) will have perspective elongation, and a Shack-Hartmann wavefront sensor (SH-WFS) subaperture image of such a laser beacon will be elongated. The degree of elongation, θ_{Na}, increases approximately proportionally to the distance between the subaperture and the laser launch telescope (LLT), the thickness of the layer, and decreases proportionally to the inverse of the square of the profile mean altitude: $\theta_{Na} \approx r_{\rm SA}\,\sigma_{\rm Na}/h_{\rm Na}^2$. For the Thirty Meter Telescope (TMT) [1], the LLT will be located behind the secondary mirror of the telescope, producing radially elongated LGS subaperture focal-plane spots. $h_{\rm Na}$, $\sigma_{\rm Na}$ and the detailed structure of the sodium profile $\mathrm{P}_{\rm Na}(h)$ all evolve significantly on time scales of seconds to minutes. For edge subapertures of the TMT ($r_{\rm SA} = 14.5$ m), the average angular size of the sodium layer along the radial direction, is on the order of $\theta_{Na} \sim 3\,\mathrm{arcsec} \geq 3\,\theta_{\rm seeing}$, which is at least 3 times larger than the seeing-limited angular size $\theta_{\rm seeing} = \lambda_{\rm WFS}/r_0(\lambda_{\rm WFS})$ of the transverse laser beacon intensity pattern at the laser focus on the sodium layer.

This paper analyzes the impact of these radially elongated and temporally varying LGS spots on the measurement accuracy, the associated wavefront error, and the linear dynamic range of the standard centroid algorithm and of a more refined noise-optimal matched filter spot position estimation algorithm for the TMT facility adaptive optics (AO) system. Results presented are based on a contiguous set of 88 LIDAR sodium profile measurements with temporal and spatial resolution of 72 sec and 24 m respectively [2]. For square subapertures of size equal to $d_{\rm SA} = 0.5$ m at the primary mirror and integration times on the order of 1 milli-second, which correspond to the TMT baseline AO system design, a 17 Watt CW sodium laser is anticipated to provide a mean photon return yielding on the order of $N = 10^3$ photo-detected electrons per sensing subaperture per integration time [3]. This level of signal is assumed throughout the paper and is the requirement currently imposed upon the TMT LGS facility.

Send correspondence to lgilles@caltech.edu

Advances in Adaptive Optics II, edited by Brent L. Ellerbroek, Domenico Bonaccini Calia,
Proc. of SPIE Vol. 6272, 62721A, (2006) · 0277-786X/06/$15 · doi: 10.1117/12.671486

It is found that the rms spot position estimation error due to noise is significantly increased at the edge of the TMT aperture due to the impact of laser guidestar elongation, but the effect can be reduced with noise optimal matched filter processing. This is particularly true when CCD read out noise is non-zero. The wavefront error for the TMT baseline AO system employing 16×4 CCD arrays per subaperture is on the order of 32 nm in absence of read noise and 45 nm with 5 electrons rms read noise per pixel per read for the matched filter algorithm. The additional root sum square (RSS) wavefront error for a centroid algorithm is on the order of 14 nm and 55 nm respectively.

In terms of linear dynamic range, the centroid algorithm provides 2-3 times more dynamic range than the matched filter, but the effect is expected to be small since (i) the null point for each LGS WFS subaperture may be calibrated to account for non-common path wavefront aberrations without dynamic range degradation, and (ii) the time-varying residual tip/tilt subaperture wavefront aberrations due to atmospheric turbulence is expected to be smaller than the dynamic ranges in question.

The paper is organized as follows: Section 2 provides an overview of the LGS SH-WFS subaperture spot model. Sub-sections 2.2 and 2.3 present respectively the centroid and the matched filter spot position estimation algorithms. Sample numerical results are presented in Section 3. Finally, Section 4 concludes the study.

2. LGS SH-WFS SPOT MODEL AND SPOT POSITION ESTIMATION ALGORITHMS

2.1. Spot Model

The LGS SH-WFS subaperture spot model developed for this study is inspired from a similar model proposed by Ellerbroek [4,5]. The continuous subaperture average spot will be denoted $i(\theta_x, \theta_y)$, where θ_x and θ_y denote the angular position coordinates in the subaperture focal-plane along the horizontal and vertical directions. In the angular frequency domain, the subaperture spot spectrum will be denoted $\widehat{i}(u_x, u_y)$, where u_x and u_y denote the angular frequency coordinates along the horizontal and vertical directions. Isoplanatic conditions are assumed to approximately hold, so that $i(\theta_x, \theta_y)$ can be modeled as the convolution of the subaperture point-spread function, denoted $\mathrm{PSF}_{\mathrm{SA}}(\theta_x, \theta_y)$, with the beacon object, denoted $i_{\mathrm{beacon}}(\theta_x, \theta_y)$:

$$i(\theta_x, \theta_y) = \mathrm{PSF}_{\mathrm{SA}}(\theta_x, \theta_y) \star i_{\mathrm{beacon}}(\theta_x, \theta_y)\,. \tag{2.1}$$

The subaperture PSF is modeled as a short-exposure Kolmogorov turbulence degraded PSF, and the beacon object as the convolution of the laser beam transverse cross-section at the laser focus on the sodium layer with a geometrical image of the sodium profile, denoted $i_{\mathrm{Na}}(\theta_x, \theta_y)$, modeling the depth of the sodium layer. Invoking reciprocity, the laser beam transverse cross-section at the laser focus on the sodium laser is modeled as the LLT aperture PSF, denoted $\mathrm{PSF}_{\mathrm{LLT}}(\theta_x, \theta_y)$. As for the sensing subaperture, the LLT PSF is modeled as a short-exposure Kolmogorov turbulence degraded PSF. We thus have:

$$i_{\mathrm{beacon}}(\theta_x, \theta_y) = \mathrm{PSF}_{\mathrm{LLT}}(\theta_x, \theta_y) \star i_{\mathrm{Na}}(\theta_x, \theta_y)\,. \tag{2.2}$$

The beacon object is proportional to the signal level, N, and is normalized such that the integral of the subaperture spot over an infinite focal plane is equal to N:

$$\int_{-\infty}^{\infty} d\theta_x \int_{-\infty}^{\infty} d\theta_y i(\theta_x, \theta_y) = N\,. \tag{2.3}$$

Invoking the convolution theorem, the angular frequency spectrum of the subaperture spot is expressed as a product of the respective spectra:

$$\widehat{i}(u_x, u_y) = \mathrm{OTF}_{\mathrm{SA}}(u_x, u_y)\, \widehat{i}_{\mathrm{beacon}}(u_x, u_y)\,, \tag{2.4}$$

$$\widehat{i}_{\mathrm{beacon}}(u_x, u_y) = \mathrm{OTF}_{\mathrm{LLT}}(u_x, u_y)\, \widehat{i}_{\mathrm{Na}}(u_x, u_y)\,. \tag{2.5}$$

The sensing subaperture and LLT aperture PSF's are modeled as the inverse Fourier transform of the respective short-exposure Kolmogorov turbulence degraded OTF's:

$$\mathrm{PSF}_{\mathrm{SA(LLT)}}(\theta_x,\theta_y;\lambda) = \frac{\mathcal{F}^{-1}\{\mathrm{OTF}_{\mathrm{SA(LLT)}}(u_x,u_y;\lambda)\}}{\int_{-\infty}^{\infty}du_x\int_{-\infty}^{\infty}du_y\mathrm{OTF}^{\mathrm{DL}}_{\mathrm{SA(LLT)}}(u_x,u_y;\lambda)}\,, \tag{2.6}$$

$$\mathrm{OTF}_{\mathrm{SA(LLT)}}(u_x,u_y;\lambda) = \frac{\int_{-\infty}^{\infty}dx\int_{-\infty}^{\infty}dy\,f_{\mathrm{SA(LLT)}}}{\int_{-\infty}^{\infty}dx\int_{-\infty}^{\infty}dy\left|U_{\mathrm{SA(LLT)}}(x,y)\right|^2}\,, \tag{2.7}$$

$$f_{\mathrm{SA(LLT)}} = U_{\mathrm{SA(LLT)}}(x,y;\lambda)\,U^{*}_{\mathrm{SA(LLT)}}(x+\lambda\,u_x,y+\lambda\,u_y;\lambda)$$
$$\times\exp(-\frac{1}{2}\,(\frac{2\pi}{\lambda})^2\,D_{\overline{\mathrm{OPD}}_{\mathrm{SA(LLT)}}}(x,y;x+\lambda\,u_x,y+\lambda\,u_y))\,, \tag{2.8}$$

where $U_{\mathrm{SA(LLT)}}$ denotes the subaperture (LLT aperture) field amplitude, $D_{\overline{\mathrm{OPD}}_{\mathrm{SA(LLT)}}}$ is the piston-tip-tilt removed Kolmogorov optical path difference (OPD) structure function, (x,y) is the spatial coordinate of a point in the subaperture (LLT aperture), and $\mathrm{OTF}^{\mathrm{DL}}_{\mathrm{SA(LLT)}}$ denotes the diffraction limited OTF's. $D_{\overline{\mathrm{OPD}}_{\mathrm{SA(LLT)}}}$ is not a shift-invariant function and must be evaluated numerically. $U_{\mathrm{SA(LLT)}}$ is expressed as follows:

$$U_{\mathrm{SA(LLT)}}(x,y;\lambda) = W_{\mathrm{SA(LLT)}}(x,y)\,\exp(j\frac{2\pi}{\lambda}\mathrm{OPD}_{\mathrm{SA(LLT)}}(x,y))\,, \tag{2.9}$$

$$W_{\mathrm{SA}}(x,y) = \mathrm{rect}(\frac{x}{d_{\mathrm{SA}}})\,\mathrm{rect}(\frac{y}{d_{\mathrm{SA}}})\,, \tag{2.10}$$

$$\mathrm{OPD}_{\mathrm{SA}}(x,y) = \theta_x^{\mathrm{ref}}\,x+\theta_y^{\mathrm{ref}}\,y+\theta_x^{\mathrm{in}}\,x+\theta_y^{\mathrm{in}}\,y\,, \tag{2.11}$$

$$W_{\mathrm{LLT}}(x,y) = \mathrm{circ}(\frac{2\sqrt{x^2+y^2}}{d_{\mathrm{LLT}}})\,\frac{\exp(-(x^2+y^2)/(2\,\sigma^2_{\mathrm{laser}}))}{2\,\pi\,\sigma^2_{\mathrm{laser}}}\,, \tag{2.12}$$

$$\mathrm{OPD}_{\mathrm{LLT}}(x,y) = 0\,, \tag{2.13}$$

where $(\theta_x^{\mathrm{ref}},\theta_y^{\mathrm{ref}})$ denotes the angular coordinates of the subaperture focal plane null point (which will be non-zero to account for WFS non-common path aberrations), and $(\theta_x^{\mathrm{in}},\theta_y^{\mathrm{in}})$ denotes the input subaperture Zernike tilt which is estimated by the centroid and matched filter spot position estimation algorithms detailed below. The $1/e^2$ laser beam intensity diameter is equal to $2\sqrt{2}\,\sigma_{\mathrm{laser}}$. The use of short-exposure Kolmogorov turbulence degraded OTF's is based on the assumption that (i) the LGS SH-WFS and laser pointing loop operate in closed loop and are perfectly tip/tilt compensated, and (ii) d_{SA} and d_{LLT} are small so that Kolmogorov statistics approximatley holds.

Finally, expressing the cartesian coordinates of a given subaperture in terms of its polar coordinates, $x_{\mathrm{SA}} = r_{\mathrm{SA}}\cos(\varphi_{\mathrm{SA}})$, $y_{\mathrm{SA}} = r_{\mathrm{SA}}\sin(\varphi_{\mathrm{SA}})$, it is convenient to introduce locally rotated angular coordinates $(\theta_{\parallel},\theta_{\perp})$, related to (θ_x,θ_y) by a rotation:

$$\begin{bmatrix}\theta_{\parallel}\\ \theta_{\perp}\end{bmatrix} = \mathrm{Rot}_{\mathrm{SA}}(-\varphi_{\mathrm{SA}})\begin{bmatrix}\theta_x\\ \theta_y\end{bmatrix}\,, \tag{2.14}$$

$$\mathrm{Rot}_{\mathrm{SA}}(\varphi_{\mathrm{SA}}) = \begin{bmatrix}\cos(\varphi_{\mathrm{SA}}) & \sin(\varphi_{\mathrm{SA}})\\ -\sin(\varphi_{\mathrm{SA}}) & \cos(\varphi_{\mathrm{SA}})\end{bmatrix}\,. \tag{2.15}$$

Note that the $\parallel$-axis points thus from the LLT to the subaperture of interest, and the $\perp$-axis is orthogonal to that direction (see Fig.1). These two directions will be refered to as radial and azimuthal in what follows. The geometrical image of the sodium profile $\mathrm{P}_{\mathrm{Na}}(h)$ at a distance r_{SA} from the LLT is then modeled as follows:

$$i_{\mathrm{Na}}(\theta_x,\theta_y) = \frac{1}{r_{\mathrm{SA}}}\,\delta(\theta_{\perp})\mathrm{P}_{\mathrm{Na}}(\,h(\theta_{\parallel})+h_{\mathrm{Na}}\,)\,, \tag{2.16}$$

$$h(\theta_{\parallel}) \approx \delta h+\frac{h^2_{\mathrm{LGS}}\,\theta_{\parallel}}{r_{\mathrm{SA}}}\,,\qquad \delta h = h_{\mathrm{LGS}}-h_{\mathrm{Na}}\,, \tag{2.17}$$

where $\theta_{\parallel}$ and $\theta_{\perp}$ are given by eq.(2.14), h_{Na} is the centroid of the sodium profile, and h_{LGS} denotes the LGS SH-WFS focus altitude.

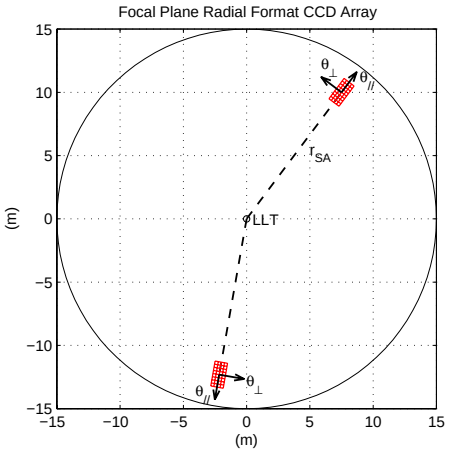

Figure 1. Illustration of subaperture focal-plane radial geometry CCD arrays.

This study addresses the impacts of the sodium layer structure and structural variability but does not address the impacts of a temporal lag on refocusing the laser to the correct mean sodium layer altitude, hence we assume in what follows that $\delta h = 0$. In the angular frequency domain, the sodium profile image spectrum is given by the following expression:

$$\widehat{i}_{\rm Na}(u_x, u_y) = \frac{1}{h_{\rm LGS}^2}\, \widehat{\rm P}_{\rm Na}(\, f = \frac{x_{\rm SA}\, u_x + y_{\rm SA}\, u_y}{h_{\rm LGS}^2}\,)\, \exp(j\, 2\pi f h_{\rm LGS})\,. \tag{2.18}$$

Higher-order effects generated by the 3D LGS that are not included in the model are speckle noise and depth of focus.

Pixel intensities *averaged over the Poisson photon arrival statistics and over the normally distributed read out noise* are obtained by integrating the continuous LGS SH-WFS subaperture spot $i(\theta_x, \theta_y)$ over each CCD pixel bin $B^{(k)}(\theta_x, \theta_y)$. In vector notation, we have:

$$\vec{I}^{\,\rm avg} = \int_{-\infty}^{\infty} d\theta_x \int_{-\infty}^{\infty} d\theta_y\, i(\theta_x, \theta_y)\, \vec{B}(\theta_x, \theta_y)\,, \tag{2.19}$$

$$= \int_{-\infty}^{\infty} du_x \int_{-\infty}^{\infty} du_y\, \widehat{i}(u_x, u_y)\, \widehat{\vec{B}}^{\,*}(u_x, u_y)\,, \tag{2.20}$$

where the last equality follows from the fact that the Fourier transform is a unitary transformation. Pixel bins are modeled as square boxes of angular subtense $\theta_{\rm pix}$, with radial and azimuthal coordinate vectors $\vec{\theta}_{\|}$ and $\vec{\theta}_{\perp}$ in the locally rotated frame, blurred by a gaussian response function modeling charge diffusion:

$$\vec{B}(\theta_x, \theta_y) = {\rm rect}(\, \frac{\theta_{\|} - \vec{\theta}_{\|}}{\theta_{\rm pix}}\,)\, {\rm rect}(\, \frac{\theta_{\perp} - \vec{\theta}_{\perp}}{\theta_{\rm pix}}\,) \star \frac{\exp(\, -(\theta_{\|}^2 + \theta_{\perp}^2)/(2\,\theta_{\rm blur}^2)\,)}{2\,\pi\,\theta_{\rm blur}^2}\,, \tag{2.21}$$

where $\theta_{\|}$ and $\theta_{\perp}$ are again given by eq.(2.14).

Noisy pixel intensities are obtained by adding a noise term to the above average pixel intensities as follows:

$$\vec{I} = \vec{I}^{\,\rm avg} + \vec{\eta}\,, \tag{2.22}$$

$$\vec{\eta} = {\rm Poisson}(\vec{I}^{\,\rm avg}) - \vec{I}^{\,\rm avg} + \sigma_e\, {\rm Normal}(\vec{0}, \mathcal{I})\,, \tag{2.23}$$

where $\mathcal{I}$ is the identity matrix. Note that $\vec{\eta}$ has a zero ensemble mean, and a diagonal covariance matrix equal to:

$$C_\eta = \langle\, \vec{\eta}\, \vec{\eta}^{\rm T}\, \rangle - \langle\, \vec{\eta}\, \rangle\, \langle\, \vec{\eta}\, \rangle^{\rm T} = {\rm diag}(\vec{I}^{\,\rm avg} + \sigma_e^2)\,. \tag{2.24}$$

A subaperture focal-plane CCD array with $N_{\rm pix}^{\parallel} \times N_{\rm pix}^{\perp}$ pixels is expressed as the sum of the individual pixel bins $B^{(k)}(\theta_x, \theta_y)$. Integrating the subaperture spot over the total field of view (FoV) of the detector array yields the average signal level multiplied by a leakage factor:

$$\vec{1}^{\rm T}\,\vec{I}^{\,\rm avg} = \int_{-\infty}^{\infty} d\theta_x \int_{-\infty}^{\infty} d\theta_y\, i(\theta_x, \theta_y)\, \vec{1}^{\rm T}\,\vec{B}(\theta_x, \theta_y) = \gamma\, N\,, \tag{2.25}$$

where $\gamma \leq 1$ is the leakage factor, i.e. the energy loss factor due to photons falling outside the CCD array. The subaperture signal-to-noise ratio (SNR) is then equal to:

$$\mathrm{SNR} \;=\; \frac{\vec{1}^{\rm T}\,\vec{I}^{\,\rm avg}}{\sqrt{\mathrm{Tr}\,(C_\eta)}} = \frac{\gamma\, N}{\sqrt{\gamma\, N + N_{\rm pix}^{\parallel}\, N_{\rm pix}^{\perp}\, \sigma_e^2}}\,. \tag{2.26}$$

2.2. Centroid Algorithm

The centroid algorithm has been extensively used in combination with 2×2 pixel arrays known as quadrant detectors or quad-cells. A detailed analysis of the algorithm's noise properties was presented in this context by Tyler and Fried in their seminal 1982 paper [6]. This material is briefly reviewed below in the framework of an arbitrary CCD array geometry with $N_{\rm pix}^{\parallel} \times N_{\rm pix}^{\perp}$ pixels and an arbitrary subaperture focal plane null point.

The centroid spot position estimate is given by the following expression:

$$\widehat{\theta}_{\parallel(\perp)}^{\rm in} \;=\; \vec{\omega}_{\parallel(\perp)}^{\rm T}\,(\alpha\,\vec{I} - \vec{I}_0^{\,\rm avg})\,, \tag{2.27}$$

$$\vec{I}_0^{\,\rm avg} \;=\; \vec{I}^{\,\rm avg}(\vec{\theta}^{\,\rm in} = \vec{0})\,, \tag{2.28}$$

$$\vec{\omega}_{\parallel(\perp)} \;=\; \frac{\theta_{\parallel(\perp)}^{\rm B}}{\vec{1}^{\rm T}\,\vec{I}_0^{\,\rm avg}}\,\vec{\theta}_{\parallel(\perp)}\,, \tag{2.29}$$

$$\alpha \;=\; \frac{\vec{1}^{\rm T}\,\vec{I}_0^{\,\rm avg}}{\vec{1}^{\rm T}\,\vec{I}}\,, \tag{2.30}$$

$$\frac{\theta_{\parallel(\perp)}^{\rm B}}{\vec{1}^{\rm T}\,\vec{I}_0^{\,\rm avg}} \;=\; \left[\,\frac{d\,\vec{\theta}_{\parallel(\perp)}^{\rm T}(\alpha^{\,\rm avg}\vec{I}^{\,\rm avg} - \vec{I}_0^{\,\rm avg})}{d\,\theta_{\parallel(\perp)}^{\rm in}}\bigg|_{\theta_{\parallel(\perp)}^{\rm in}=0}\,\right]^{-1} \approx \frac{1}{\vec{g}_{\parallel(\perp)}^{\rm T}\,\vec{\theta}_{\parallel(\perp)}}\,, \tag{2.31}$$

$$\vec{g}_{\parallel(\perp)} \;=\; \frac{\partial\,\vec{I}^{\,\rm avg}}{\partial\,\theta_{\parallel(\perp)}^{\rm in}}\bigg|_{\theta_{\parallel(\perp)}^{\rm in}=0}\,. \tag{2.32}$$

$\theta_{\parallel(\perp)}^{\rm B}$ in (2.29) and $\vec{g}_{\parallel(\perp)}$ in (2.32) denote respectively the centroid gain and the radial and azimuthal slopes of the average pixel intensity transfer curves at null. The later can be estimated in practice by continually dithering the laser beacon on the sky, and can be updated on slow time scales of a few seconds.

It should be pointed out that a spot position estimation bias occurs in the radial direction if the centroid algorithm is not updated rapidly enough to track the variations in the shape of the sodium profile. Mathematically, this bias is expressed as follows:

$$\widehat{\theta}_{\rm bias}(t; t+\delta) \;=\; \vec{\omega}_{\parallel(\perp)}^{\rm T}(t)\;(\,\alpha(t; t+\delta)\vec{I}_0^{\,\rm avg}(t+\delta) - \vec{I}_0^{\,\rm avg}(t)\,)\,, \tag{2.33}$$

$$\alpha(t; t+\delta) \;=\; \frac{\vec{1}^{\rm T}\,\vec{I}_0^{\,\rm avg}(t)}{\vec{1}^{\rm T}\,\vec{I}_0^{\,\rm avg}(t+\delta)}\,. \tag{2.34}$$

Note that if $\vec{I}_0^{\,\rm avg}(t+\delta)$ is simply proportional to $\vec{I}_0^{\,\rm avg}(t)$, the spot position estimation bias is equal to zero. A rough estimate of the telescope full-aperture wavefront error due to a non-zero bias can be obtained by reconstructing

the wavefront at the subaperture resolution and summing up radially the biases for each subaperture from the LLT to the edge of the aperture. In integral notation, this is expressed as follows:

$$\widehat{\phi}_{\rm bias}(r) \;=\; \int_0^r dr'\,\widehat{\theta}_{\rm bias}(r')\,. \tag{2.35}$$

Piston removed and piston-focus removed wavefronts can then be computed using the usual formula:

$$\widehat{\phi}^{(1)}_{\rm bias}(r) = \widehat{\phi}_{\rm bias}(r) - c_1\,Z_1\left(\frac{2r}{D}\right)\,, \tag{2.36}$$

$$\widehat{\phi}^{(4)}_{\rm bias}(r) = \widehat{\phi}^{(1)}_{\rm bias}(r) - c_4\,Z_4\left(\frac{2r}{D}\right)\,, \tag{2.37}$$

$$c_{1(4)} = \frac{\int_0^{2\pi} d\,\varphi\,\int_0^{D/2} r\,dr\,\widehat{\phi}_{\rm bias}(r)\,Z_{1(4)}\,(2r/D)}{\pi D^2/4}\,, \tag{2.38}$$

where $Z1(4)$ denote the Zernike piston and focus modes. The rms error due to the biases is finally expressed as:

$$\sigma^2_{1(4)} \;=\; \frac{\int_0^{2\pi} d\,\varphi\,\int_0^{D/2} r\,dr\,\left[\,\widehat{\phi}^{1(4)}_{\rm bias}(r)\right]^2}{\pi D^2/4}\,. \tag{2.39}$$

Due to photon and read out noise, the centroid estimate (2.27) is a random variable, whose variance at the null point, known as the centroid noise propagation, is equal to the following expression:

$$\sigma^2_{\vec{\theta}_{\parallel(\perp)}} \;=\; \left(\frac{\theta^{\rm B}_{\parallel(\perp)}}{\vec{1}^{\rm T}\,\vec{I}_0^{\,\rm avg}}\right)^2 {\rm var}\left[\,\vec{\theta}^{\rm T}_{\parallel(\perp)}(\alpha\,\vec{I}_0^{\,\rm avg} + \alpha\,\vec{\eta} - \vec{I}_0^{\,\rm avg})\right]\,, \tag{2.40}$$

$$\alpha \;=\; \frac{1}{1+\epsilon} \approx 1-\epsilon\,, \tag{2.41}$$

$$\epsilon \;=\; \frac{\vec{1}^{\rm T}\,\eta}{\vec{1}^{\rm T}\,\vec{I}_0^{\,\rm avg}}\,. \tag{2.42}$$

After a little algebra, the following expression is obtained:

$$\sigma^2_{\vec{\theta}_{\parallel(\perp)}} \;=\; \left(\theta^{\rm B}_{\parallel(\perp)}\right)^2\left[\frac{\xi_{\parallel(\perp)}}{{\rm SNR}^2(\vec{\theta}^{\rm in}=\vec{0})} + \frac{q^2_{\parallel(\perp)}}{{\rm SNR}^2(\vec{\theta}^{\rm in}=\vec{0})} - 2\,\frac{q^2_{\parallel(\perp)}}{\vec{1}^{\rm T}\,\vec{I}_0^{\,\rm avg}}\right]\,, \tag{2.43}$$

$$q_{\parallel(\perp)} \;=\; \vec{\theta}^{\rm T}_{\parallel(\perp)}\,\frac{\vec{I}_0^{\,\rm avg}}{\vec{1}^{\rm T}\,\vec{I}_0^{\,\rm avg}}\,, \tag{2.44}$$

$$\xi_{\parallel(\perp)} \;=\; \frac{{\rm Tr}(\,\vec{\theta}_{\parallel(\perp)}\,\vec{\theta}^{\rm T}_{\parallel(\perp)}\,C_{\rm mod}\,)}{{\rm Tr}(\,C_{\rm mod}\,)} = \frac{\sum_k(\,\theta^{(k)}_{\parallel(\perp)}\,)^2\,(\,I_0^{\,{\rm avg}(k)} + \sigma_e^2\,)}{\sum_k(\,I_0^{\,{\rm avg}(k)} + \sigma_e^2\,)}\,, \tag{2.45}$$

$$C_{\rm mod} \;=\; C_\eta(\vec{\theta}^{\rm in}=\vec{0})\,. \tag{2.46}$$

Note that for a quadrant detector, $\xi_{\parallel(\perp)}$ is simply equal to a quarter of a pixel area.

2.3. Matched Filter Algorithm

We define a matched filter algorithm by the following *noise-weighted least-squares* optimization problem:

$$(\widehat{\theta^{\rm in}_\parallel}, \widehat{\theta^{\rm in}_\perp}, \widehat{\delta N}) \;=\; \arg\min_{(\theta^{\rm in}_\parallel,\theta^{\rm in}_\perp,\delta N)} J(\theta^{\rm in}_\parallel,\theta^{\rm in}_\perp,\delta N)\,, \tag{2.47}$$

$$J(\theta^{\rm in}_\parallel,\theta^{\rm in}_\perp,\delta N) \;=\; \vec{y}^{\rm T}\,C^{-1}_{\rm mod}\,\vec{y}\,, \tag{2.48}$$

$$\vec{y} \;=\; \vec{I} - (\vec{I}_0^{\,\rm avg} + \vec{g}_\parallel\,\theta^{\rm in}_\parallel + \vec{g}_\perp\,\theta^{\rm in}_\perp + \frac{\vec{I}_0^{\,\rm avg}}{N}\,\delta N)\,, \tag{2.49}$$

$$C_{\rm mod} \;=\; C_\eta(\theta^{\rm in}_\parallel = 0, \theta^{\rm in}_\perp = 0, \delta N = 0)\,, \tag{2.50}$$

where $\vec{g}_{\parallel(\perp)}$ are given by eq.(2.32).

The solution for $\widehat{\theta^{\rm in}_{\parallel}}$ and $\widehat{\theta^{\rm in}_{\perp}}$ is given by the following expressions:

$$\widehat{\theta}^{\rm in}_{\parallel(\perp)} = \vec{\omega}^{\rm T}_{\parallel(\perp)} \left(\vec{I} - \vec{I}_0^{\rm avg}\right), \tag{2.51}$$

$$\vec{\omega}_{\parallel} = \sigma^2_{\theta_{\parallel}} C^{-1}_{\rm mod} \left(\vec{g}_{\parallel} - \mu\, \vec{I}_0^{\rm avg}\right), \tag{2.52}$$

$$\mu = \frac{\vec{g}^{\rm T}_{\parallel} C^{-1}_{\rm mod} \vec{I}_0^{\rm avg}}{\vec{I}_0^{\rm avg\,T} C^{-1}_{\rm mod} \vec{I}_0^{\rm avg}}, \tag{2.53}$$

$$\vec{\omega}_{\perp} = \sigma^2_{\theta_{\perp}} C^{-1}_{\rm mod}\, \vec{g}_{\perp}\,. \tag{2.54}$$

The matched filter noise propagation coefficients are expressed as follows:

$$\sigma^2_{\theta_{\parallel}} = \frac{1}{\vec{g}^{\rm T}_{\parallel} C^{-1}_{\rm mod} \left(\vec{g}_{\parallel} - \mu\, \vec{I}_0^{\rm avg}\right)}, \tag{2.55}$$

$$\sigma^2_{\theta_{\perp}} = \frac{1}{\vec{g}^{\rm T}_{\perp} C^{-1}_{\rm mod}\, \vec{g}_{\perp}}\,. \tag{2.56}$$

Equations (2.51)-(2.56) follow from the following symmetries of vectors $\vec{g}_{\parallel}$, $\vec{g}_{\perp}$, and $\vec{I}_0^{\rm avg}$ when displayed as $N^{\parallel}_{\rm pix} \times N^{\perp}_{\rm pix}$ arrays:

1. array($\vec{g}_{\parallel}$) is symmetric along the $\perp$-direction, i.e. its rows are identical.
2. array($\vec{g}_{\perp}$) is anti-symmetric along the $\perp$-direction, i.e. $\vec{g}^{\rm T}_{\perp}\, \vec{1} = 0$. In particular, $\vec{g}^{\rm T}_{\perp}\, \vec{g}_{\parallel} = 0$.
3. array($\vec{I}_0^{\rm avg}$) is symmetric along the $\perp$-direction, i.e. its rows are identical. In particular, $\vec{g}^{\rm T}_{\perp} C^{-1}_{\rm mod} \vec{I}_0^{\rm avg} = \vec{g}^{\rm T}_{\perp} C^{-1}_{\rm mod} \vec{g}_{\parallel} = 0$.

Finally, as for the centroid algorithm, a spot position estimation bias occurs in the radial direction if the matched filter algorithm is not updated rapidly enough to track the variations in the shape of the sodium profile. Note that the parameter μ in (2.52) ensures that $\widehat{\theta}_{\rm bias} = 0$ and $\widehat{\delta N} = \delta N$ if $\vec{I} = (N + \delta N)/N\, \vec{I}_0^{\rm avg}$.

3. SIMULATION RESULTS

Fig.2 displays the mean sodium profile obtained by averaging and centering 88 contiguous frames of LIDAR measurements with spatial resolution equal to 24 m [2] as well as a sample sodium profile frame.

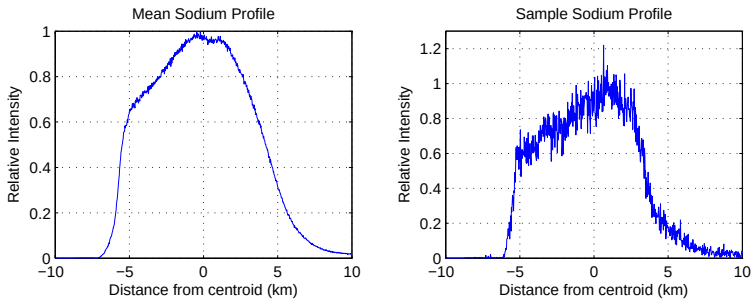

Figure 2. Left panel: mean sodium profile obtained by averaging and centering 88 contiguous frames of LIDAR measurements of the sodium layer with spatial resolution equal to 24 m [2]. Right panel: sample sodium profile frame.

Fig.3 displays Nyquist sampled short-exposure subaperture and LLT aperture PSF's. The subaperture size was taken equal to $d_{\rm SA} = 0.5$ m (order 60×60 wavefront sensor), the LLT diameter equal to $d_{\rm LLT} = d_{\rm SA} = 0.5$ m, and the $1/e^2$ gaussian laser beam intensity diameter equal to $0.6\, d_{\rm LLT} = 0.3$ m. The Fried parameter was chosen equal to $r_0(\lambda_0 = 500\,{\rm nm}) = 0.15$ m. Note that the LLT Strehl ratio (SR) is in excellent agreement with Maréchal's approximation, ${\rm SR}(\lambda_{\rm WFS}) \approx \exp(-\sigma^2)$, where $\sigma^2 = 0.134(d_{\rm LLT}/r_0(\lambda_{\rm WFS}))^{5/3}$ is the piston-tip-tilt removed Kolmogorov phase variance in radians squared. PSF's were computed in the Fourier domain using 64×64 FFT grids.

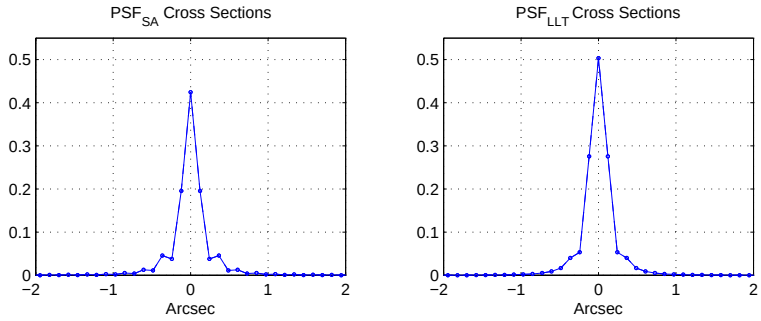

Figure 3. Left panel: Nyquist sampled subaperture short-exposure PSF. Right panel: Nyquist sampled LLT aperture short-exposure PSF. The subaperture size was taken equal to $d_{\rm SA} = 0.5$ m (order 60×60 wavefront sensor), the LLT diameter equal to $d_{\rm LLT} = d_{\rm SA} = 0.5$ m, and the $1/e^2$ gaussian laser beam diameter equal to $0.6\, d_{\rm LLT} = 0.3$ m. These quantities were computed in the Fourier domain using a 32×32 subaperture grid embedded into a 64×64 FFT grid. The Fried parameter is $r_0(\lambda_0 = 500\,{\rm nm}) = 0.15$ m and the turbulence outer-scale is infinite.

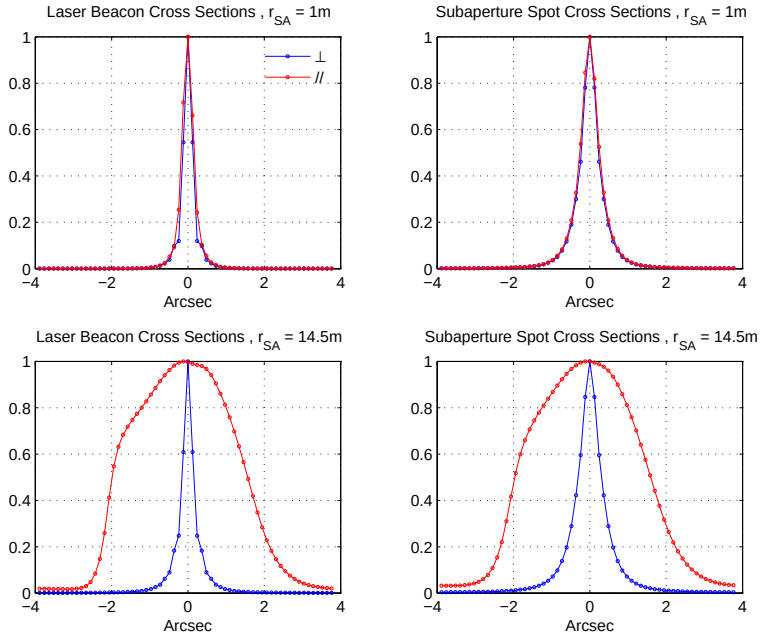

Figure 4. Left panels: Nyquist sampled normalized average beacon radial and azimuthal cross-sections as seen from a subaperture 1 m and 14.5 m away from the LLT. Right panels: total subaperture spot obtained by convolving the beacon with the short-exposure subaperture PSF.

Fig.4 displays Nyquist sampled normalized average beacon radial and azimuthal cross-sections as seen from a subaperture 1 m and 14.5 m away from the LLT, together with the total subaperture spot obtained by

convolving the beacon with the short-exposure subaperture PSF. The full width half max (FWHM) of the radial and azimuthal cross-sections of the edge subaperture spot is on the order of 3.5 arcsec and 0.8 arcsec respectively.

Fig.5 shows radial and azimuthal rms noise propagation levels for the matched filter and centroid spot position estimators, as a function of subaperture-to-LLT separation. These curves are for the median sodium profile displayed in Fig.2. The beacon brightness has been scaled to provide a mean signal level of $N = 10^3$ photo-detected electrons per subaperture per integration time, which is the requirement currently imposed upon the TMT LGS facility, and the cases of $\sigma_e = 0$ and $\sigma_e = 5$ electrons rms read out noise are compared for a 16×4 subaperture focal-plane CCD pixel array with $\theta_{\rm pix} = 0.5$ arcsec pixel subtense and $\theta_{\rm blur} = \theta_{\rm pix}/4$ pixel blurring modeling charge diffusion. The corresponding SNR's are on the order of 31 and 19 respectively. It is seen that the spot position estimation error due to noise is significantly increased at the edge of the TMT aperture due to the impact of laser guidestar elongation, but the effect can be reduced through the use of the noise-optimal matched filter. This is particularly true when the detector read out noise is non-zero. It is also seen that shifting the null point from the origin (center) of the subaperture focal plane to half a pixel in both radial and azimuthal directions (as might be the case with sample non-common path wavefront errors) only marginally degrades the noise properties of the algorithms.

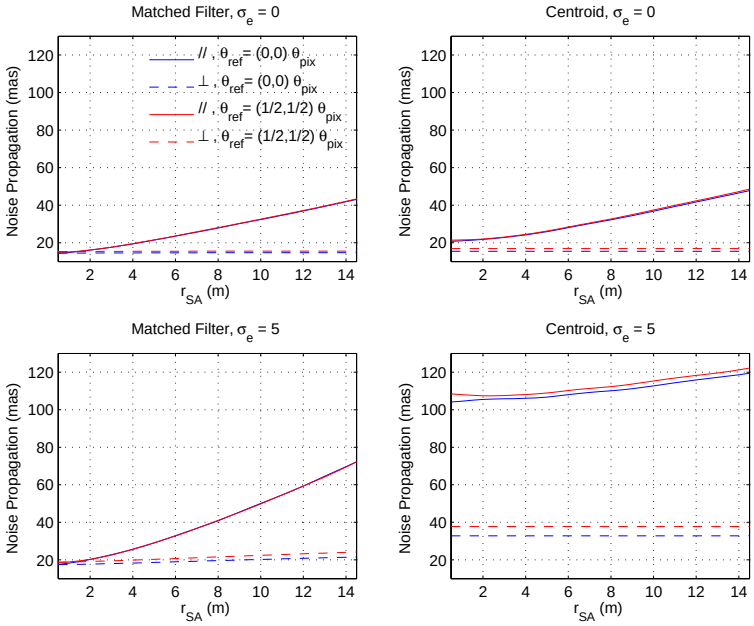

Figure 5. Radial and azimuthal photon and read out noise propagation levels associated to the matched filter and centroid spot position estimators, as a function of the subaperture-to-LLT separation. These curves are for the median sodium profile displayed in Fig.2. The beacon brightness has been scaled to provide a mean signal level equal to $N = 10^3$ photo-detected electrons per subaperture per integration time, and the cases of $\sigma_e = 0$ and $\sigma_e = 5$ electrons rms read out noise are compared for a 16×4 subaperture focal-plane CCD pixel array with $\theta_{\rm pix} = 0.5$ arcsec pixel subtense and $\theta_{\rm blur} = \theta_{\rm pix}/4$ pixel blurring due to charge diffusion. The corresponding SNR's are on the order of 31 and 19 respectively. Blue and red curves refer to the null point set respectively at the origin (center) of the subaperture focal plane and at a null position shifted by a quarter pixel in both radial and azimuthal directions (as might be the case with sample non-common path wavefront errors). It is seen that such a null point offset has no impact on the noise properties of the algorithms.

These results are summarized for a central and an edge subaperture in Table 1. The wavefront error due to the noise has been computed for the TMT facility AO system and is displayed in Table 2. The sytem consists of 5 LGS's in a 35 arcsec radius and 1 LGS on-axis, order 60×60 sensing and correction (0.5 m subapertures and 0.5 m actuator pitch), 16×4 CCD arrays per subaperture, 1 tip-tilt-focus natural guide star WFS on-axis and

2 deformable mirrors conjugate to ground and 12 km respectively. Wavefront control is done using a double-pole integrator with a gain of 0.5 operating in pseudo open loop [7]. The error budget has been computed by substracting in quadrature noise-free from noisy closed loop Monte Carlo simulation results using the same mean sodium profile as in Fig.5. Noise-free simulations were run with a minimum variance wavefront reconstructor incorporating 15 mas subaperture regularization noise. The wavefront error is on the order of 32 nm in absence of read noise and 45 nm with 5 electrons rms read noise per pixel per read for the matched filter algorithm. The additional root sum square (RSS) wavefront error for a centroid algorithm is on the order of 14 nm and 55 nm respectively.

Table 1. Radial, azimuthal and root sum square (RSS) photon and read out noise propagation levels at $r_{\rm SA} = 0.5$ m and $r_{\rm SA} = 14.5$ m for the centroid and matched filter spot position estimators operating on the same CCD array and mean signal level as in Fig.5.

Spot position estimation algorithm	Read noise per pixel per read (electrons)	Measurement noise (mas) central subaperture			Measurement noise (mas) edge subaperture		
		Radial	Azimuthal	RSS	Radial	Azimuthal	RSS
Centroid	0	21	16	26	48	16	50
	5	104	33	109	119	33	124
Matched Filter	0	15	15	21	43	15	46
	5	18	18	25	72	22	76

Table 2. Wavefront error for the TMT facility AO system due to LGS WFS noise for the same signal level, subaperture and CCD geometry, and mean sodium profile as in Fig.5. The error budget was obtained by substracting in quadrature noise-free from noisy closed-loop Monte Carlo simulation results. Noise-free simulations were run with a minimum variance wavefront reconstructor incorporating 15 mas subaperture regularization noise.

Spot position estimation algorithm	Read noise per pixel per read (electrons)	Wavefront Error (nm) due to LGS WFS noise	
		On-Axis	10 arcsec Fov Average
Centroid	0	35	32
	5	71	67
Matched Filter	0	32	30
	5	45	42

Figure 6 displays the average spot position estimation error, $\widehat{\theta}_{\parallel(\perp)} - \theta^{\rm in}_{\parallel(\perp)}$, for a central and an edge subaperture as a function of input subaperture tilt level when the null point is set at half a pixel in both radial and azimuthal directions. The curves for the matched filter algorithm are for a mean signal level of 1000 photo-detected electrons per subaperture and per integration time and a read noise of either 0 or 5 electrons rms. For the centroid algorithm, the curves are independent of signal and read noise levels since the algorithm does not incorporate statistical prior information. The linear dynamic range of the matched filter algorithm is approximately from -100 mas to +100 mas, i.e. approximately from $-\sigma_\alpha/2$ to $+\sigma_\alpha/2$, where σ_α denotes the rms angle of arrival fluctuations over a subaperture of size $d_{\rm SA}$, i.e. $\sigma_\alpha = {\rm PV}_{\rm OPD}/d_{\rm SA}$ with ${\rm PV}_{\rm OPD} = \lambda/(2\pi)\, 4\, \langle a_2^2 \rangle^{1/2}$ and $\langle a_2^2 \rangle = 0.448\, (d_{\rm SA}/r_0)^{5/3}$. Note that these are open-loop results for a single LGS WFS subaperture. The resulting wavefront error for a closed loop AO system is expected to be small and will be evaluated using a full wave optics Monte Carlo simulation. The centroid algorithm provides 2-3 times more dynamic range, but the effect is expected to be small. Indeed, shifting the null point to a quarter pixel in both radial and azimuthal directions has no impact on these average spot position estimation error curves. The null point for each LGS WFS subaperture may thus be calibrated to account for non-common path wavefront aberrations without dynamic range degradation. Moreover, the time-varying residual subaperture wavefront tip/tilt aberrations due to atmospheric turbulence will be smaller than the dynamic ranges quoted above.

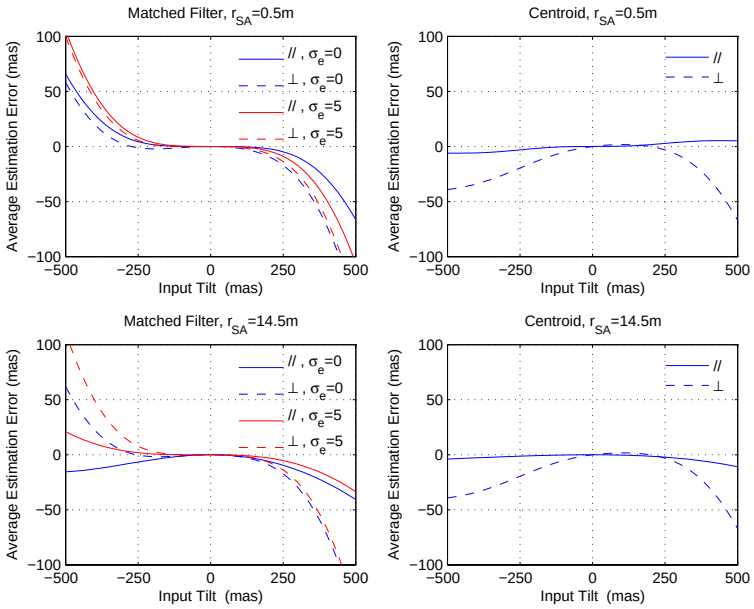

Figure 6. Average spot position estimation error curves, $\widehat{\theta}_{\parallel(\perp)} - \theta^{\text{in}}_{\parallel(\perp)}$, for a central and an edge subaperture as a function of input tilt level when the null point of the subaperture focal plane is at half a pixel in both radial and azimuthal directions. The curves for the matched filter algorithm are for a mean signal level of 1000 photo-detected electrons per subaperture and per integration time and a read noise of either 0 or 5 electrons rms. For the centroid algorithm, the curves are independent of signal and read noise levels since the algorithm does not incorporate statistical prior information.

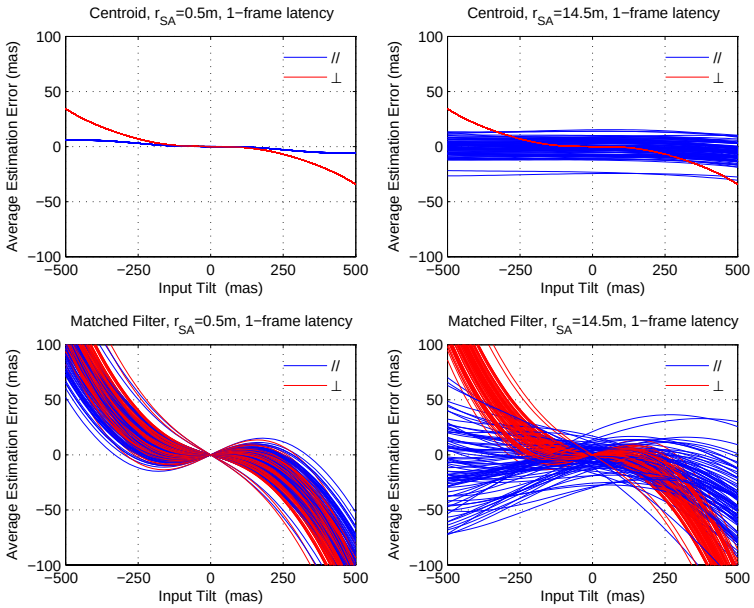

Figure 7. Average spot position estimation error curves, $\widehat{\theta}_{\parallel(\perp)} - \theta^{\text{in}}_{\parallel(\perp)}$, for a central and an edge subaperture for the centroid and matched filter algorithms as a function of input tilt level when the null point of the subaperture focal plane is at the origin and the algorithms have 72 sec (i.e. 1 frame) update latency. The different curves correspond to the 87 different pairs of contiguous sodium profile frames. The azimuthal curves are identical for all pairs of profiles for the centroid algorithm as a consequence of the symmetry properties of the algorithm.

Finally, Fig.7 illustrates sample average spot position estimation error curves for the centroid and matched filter algorithms with 72 sec (i.e. 1 frame) update latency. The azimuthal curves are identical for all pairs of profiles for the centroid algorithm as a consequence of the symmetry properties of the algorithm. The rms bias is on the order of 10 mas at $r_{\mathrm{SA}} = 14.5$ m for both algorithms. The full-aperture wavefront error corresponding to this rms bias as given by eq.(2.39) is approximately equal to 92 nm. Most of this wavefront error is a focus error. Indeed, the focus removed wavefront error is approximately equal to 12 nm only.

4. CONCLUSION

Sodium LGS SH-WFS spot elongation is a significant challenge for future extremely large telescopes such as the TMT. The LGS angular spot size along the elongation direction at the edge of the TMT exceeds 3 times the angular size of the seeing-limited transverse laser beacon intensity at the laser focus on the sodium layer. Possible approaches to defeat this effect include (i) radial-format CCD's [8] combined with a noise-optimal spot position estimation algorithm [4,5] and (ii) dynamic refocusing. This paper discussed the first approach. Using a contiguous set of LIDAR measurements of the sodium profile, the performance of a standard centroid and a more refined noise-optimal matched filter spot position estimation algorithm were analyzed and compared for a nominal mean signal level equal to 1000 photo-detected electrons per subaperture per integration time, as a function of subaperture to laser launch telescope separation distance and CCD pixel read out noise. Both algorithms were compared in terms of their average spot position estimation error due to noise, their wavefront error budget for the Thirty Meter Telescope facility adaptive optics system, their linear dynamic range and their bias when detuned from the current sodium profile.

Acknowledgments

Authors acknowledge the Purple Crow Lidar team from the University of Western Ontaria, Canada, for making their sodium layer measurements available to us. Glen Herriot and Jean-Pierre Véran from Herzberg Institute of Astronomy, Canada, are also acknowledged for fruitful discussions. The authors gratefully acknowledge the support of the TMT partner institutions. They are the Association of Canadian Universities for Research in Astronomy (ACURA), the Association of Universities for Research in Astronomy (AURA), the California Institute of Technology and the University of California. This work was supported, as well, by the Canada Foundation for Innovation, the Gordon and Betty Moore Foundation, the National Optical Astronomy Observatory, which is operated by AURA under cooperative agreement with the National Science Foundation, the Ontario Ministry of Research and Innovation, and the National Research Council of Canada.

REFERENCES

1. J.E.Nelson and G.H.Sanders, "TMT status report," in Ground-based and Airborne Telescopes, L. M. Stepp, ed., Proc. SPIE **6267,** (2006).
2. P.S.Argall, R.J.Sica, O.Vassiliev and M.M.Mwangi, "Lidar measurements taken with a large-aperture liquid mirror: Sodium resonance-fluorescence system," Appl. Opt. **39,** 2393–2399 (2000).
3. C.d'Orgeville, F.Rigaut and B.L.Ellerbroek, "LGS AO photon return simulations and laser requirements for the Gemini LGS AO program," Gemini Observatory preprint #55, available online at www.gemini.edu/documentation/webdocs/preprints/gpre55.pdf
4. B.L.Ellerbroek and G.M.Cochran, "A waveoptics propagation code for multi-conjugate adaptive optics," Proc. SPIE **4494,** 104–120 (2002).
5. B.L.Ellerbroek, "Wavefront reconstruction algorithms and simulation results for multi-conjugate adaptive optics on giant telescopes," Proc. SPIE **5382,** 478–489 (2003).
6. G.A.Tyler and D.L.Fried, "Image-position error associated with a quadrant detector," J. Opt. Soc. Am. **72**, 804–808 (1982).
7. L.Gilles, "Closed-loop stability and performance analysis of least-squares and minimum-variance control algorithms for multiconjugate adaptive optics," Appl. Opt. **44**, 993-1002 (2005).
8. J.W.Beletic, "Follow the Yellow-Orange Rabbit: A CCD optimized for wavefront sensing a pulsed sodium laser guide star," Proc. SPIE **5499,** 302–309 (2004).